Journal of Alloys and Compounds 501 (2010) 236–244

Contents lists available at ScienceDirect

Journal of Alloys and Compounds

journal homepage: www.elsevier.com/locate/jallcom

Studies of $Ti_{1.5}Zr_{5.5}V_{0.5}(M_xNi_{1-x})_{9.5}$ (M = Cr, Mn, Fe, Co, Cu, Al): Part 1. Structural characteristics

K. Young[a,*], T. Ouchi[a], B. Huang[a], J. Nei[b], M.A. Fetcenko[a]

[a] Energy Conversion Devices Inc./Ovonic Battery Company, 2983 Waterview Drive, Rochester Hills, MI 48309, USA
[b] Department of Chemical Engineering, Wayne State University, Detroit, MI 48202, USA

ARTICLE INFO

Article history:
Received 12 March 2010
Received in revised form 1 April 2010
Accepted 8 April 2010
Available online 21 April 2010

Keywords:
Hydrogen absorbing materials
Transition metal alloys
Metal hydride electrode

ABSTRACT

In Part 1 of this two part series of papers, the structural characteristics of quinary alloys $Ti_{1.5}Zr_{5.5}V_{0.5}(M_xNi_{1-x})_{9.5}$ with M = Cr, Mn, Fe, Co, Cu, or Al and $x = 0.1$ or 0.2 are reported. All 12 alloys are composed of Laves phases (C14 or C15) and non-Laves Zr–Ni phases. Only partial Cu-substitution retains a Zr_7Ni_{10}-dominated microstructure. Substitutions of elements with fewer outer shell electrons, such as Al, Mn, and Cr, were found to promote more C14 phase while Fe- and Co-substitutions favored the C15 structure. Average electron density was found to have a determining role in the predilection toward C14/C15 phases. As the Ni-content in the alloy decreases, the structure of non-Laves phase changes from Zr_7Ni_{10} to $Zr_7Ni_{10} + Zr_9Ni_{11}$, then to Zr_9Ni_{11}, and finally to $Zr_9Ni_{11} + ZrNi$. The solubilities of V and Cr in the Zr_7Ni_{10} and Zr_9Ni_{11} phases are very low and the contents of other substitutional elements in these phases are lower than in the Laves phases.

1. Introduction

The pursuit of a Zr–Ni based alloy having a stoichiometry other than AB_2 for use as the metal hydride (MH) electrode active material in nickel metal hydride (Ni/MH) battery began with Zr_7Ni_{10} intermetallic alloy [1–11]. The hydrogen-to-metal bond strength of Zr_7Ni_{10} is higher than that of the commonly used Zr-based AB_2 alloy based on the higher Zr-to-Ni ratio (0.7) of Zr_7Ni_{10}. The advantage of higher bond strength in such an alloy is the possibility of obtaining higher storage capacity in a more stable hydride [12,13]. The risk is the alloy will have a plateau pressure which is too low, thereby making hydride dissociation more difficult [7,10,11]. Therefore, alloying the Zr_7Ni_{10} composition with more elements is necessary to improve the electrochemical properties. In a previously published paper, we reported the structure and electrochemical properties of the ternary $Ti_xZr_{7-x}Ni_{10}$ alloy family (x between 0 and 2.5) [14]. As the Ti content in the alloys increases, the crystal structure (mainly a Zr_7Ni_{10} orthorhombic structure mixed with some C15 and ZrO_2 secondary phases) remains unchanged, the lattice constants decrease, the pressure–concentration–temperature (PCT) plateau pressure increases, activation becomes easier, and the high rate dischargeability (HRD) improves. In this series of alloys, ZN04 ($Ti_{1.5}Zr_{5.5}Ni_{10}$) was chosen as the base alloy for the next series of experiments on the quaternary alloy because it had a good combination of capacity and HRD.

In another previously published paper of Zr_7Ni_{10} series alloys, vanadium was added to $Ti_{1.5}Zr_{5.5}V_xNi_{10-x}$ (x between 0 and 3.0) to study the phase structure and electrochemical properties changes [15]. The V-containing alloys all show multi-phase structures. The major phase shifts from Zr_7Ni_{10} to Zr_9Ni_{11} and finally to a C14 structure as the vanadium content increases. Other minor phases including C15 and ZrNi crystal structures are also present. The bulk hydrogen transport property of the alloys is improved by synergetic effects between the major and minor phases. Electrochemical testing shows the highest discharge capacity of 357 mAh/g obtained from an alloy having a composition of $Ti_{1.5}Zr_{5.5}V_{2.5}Ni_{7.5}$. However, it is to be noted the structure of the main phase in this alloy is C14.

In this study, we continued the study of the Zr_7Ni_{10}-structured alloy by adding a fifth element. The alloy ZN07 ($Ti_{1.5}Zr_{5.5}V_{0.5}Ni_{9.5}$) with a structure of mainly Zr_7Ni_{10} phase was chosen as the base alloy.

In this two-part report, 10% and 20% of Ni in the base alloy $Zr_{5.5}Ti_{1.5}V_{0.5}Ni_{9.5}$ was replaced by a fifth element chosen from the group consisting of Cr, Mn, Fe, Co, Cu, and Al. The changes in structural properties are reported in Part I, and changes in gas phase storage and electrochemical properties are reported in Part II [16]. These inexpensive elements are commonly used as modifiers in Laves phase alloy development work. Previous publications related to Zr-based AB_2 alloy modifications by Cr, Mn, Fe, Co, and Al were reviewed [17–21]. In summary: Cr and Al extend cycle life; Mn facilitates the formation process; Fe improves cycle life, increases plateau pressure, reduces capacity, improves HRD performance in small amounts followed by reduction in HRD at higher concentrations; Co reduces PCT hysteresis and extends the cycle life; and

* Corresponding author. Tel.: +1 248 293 7000; fax: +1 248 299 4520.
E-mail address: kwoyoung@yahoo.com (K. Young).

0925-8388/$ – see front matter © 2010 Elsevier B.V. All rights reserved.
doi:10.1016/j.jallcom.2010.04.077

a combination of Co and Al may improve all major Ni/MH battery performance characteristics. Compared to the modifiers mentioned above, Cu is less commonly used in Laves phase alloys. Cu was first added to $TiCr_2$ in order to reduce annealing time and reduce the operational temperature thereof [22]. As Cu content in the alloy $Zr(Cr_{1-x}Cu_x)_2$ increases, plateau pressure increases and hydrogen storage capacity decreases [23]. Similar results were reported with $TiMn_2$-based alloys [24], where Mn was partially replaced with Cu, and Ti–Zr–Cr–V based BCC alloys [25], where the parent alloy system was substituted with Cu. Moreover, in gas phase hydrogen storage, Cu flattens the PCT isotherm [24,26] and increases the heat of formation of the hydride [27]. The addition of Cu decreases the electrochemical capacity [28,29] and reduces cycle life [30]. Cu is also reported to stabilize the C14 structure in $ZrMn_2$-based alloys [31] and to promote the C14 structure in $ZrCr_2$-based alloys [23]. In AB_5 alloys, the addition of Cu was found to be detrimental to cycle life due to the flattening of the unit cell along the *c*-axis [32], but improved low temperature specific power by altering the microstructure of the surface oxide and the imbedded metallic clusters within the surface oxide layer [33]. Also, the hydrogen storage characteristic of ZiNi alloy (B33 structure) with partial replacement of nickel by one of the transition metals (V, Cr, Mn, Fe, and Co) was previously studied [34]. In this series of alloys, the equilibrium plateau pressure has a linear dependence on the unit cell volume, and lighter substituting elements (V, Cr, and Mn) have a stronger influence on the microstructure pushing it toward the Laves phases [34].

2. Experimental setup

Samples were made by arc melting under a continuous argon flow with a non-consumable tungsten electrode and a water-cooled copper tray. Before each arc melt, a piece of sacrificial titanium underwent a few melting-cooling cycles to reduce the residual oxygen concentration in the system. Each 10-gram sample ingot was re-melted and flipped over a few times to ensure uniformity in chemical composition. The chemical composition of each sample was examined by a Varian *Liberty* 100 inductively coupled plasma (ICP) system. A Philips *X'Pert Pro* X-ray Diffractometer (XRD) was used to study each alloy's microstructure. A JOEL-*JSM6320F* Scanning Electron Microscope (SEM) with Energy Dispersive Spectroscopy (EDS) capability and a Hitachi S-2400 SEM with EDS, Backscattering Electron Image (BEI), and Electron Backscattering Diffraction (EBSD) capabilities were used to study the microstructure and composition of each alloy.

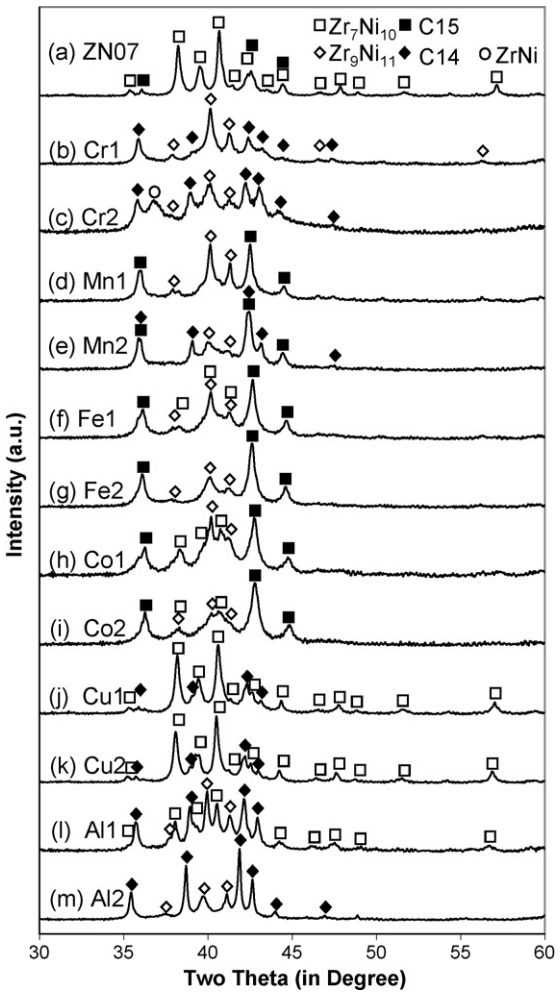

Fig. 1. XRD spectra using Cu Kα as the radiation source for as-prepared alloys ZN07 (a), Cr1 (b), Cr2 (c), Mn1 (d), Mn2 (e), Fe1 (f), Fe2 (g), Co1 (h), Co2 (i), Cu1 (j), Cu2 (k), Al1 (l), and Al2 (m).

3. Results and discussion

Twelve alloys were prepared by arc melt without any annealing treatment. Target compositions of these alloys (general formula $Ti_{1.5}Zr_{5.5}V_{0.5}(M_xNi_{1-x})_{9.5}$ with M = Cr, Mn, Fe, Co, Cu, or Al and $x = 0.1$ or 0.2) are listed in Table 1. The final chemical composition of each sample was verified by ICP to be within 0.1 wt% from the designed values.

3.1. Phase analysis by XRD study

Fig. 1 compares the XRD spectra for the 12 as-prepared alloys (with no further processing) with the spectrum of the ZN07 base alloy. The identified structures together with lattice constants and relative abundances (calculated by the Rietveld method) are listed in Table 1. The main phase shifts from Zr_7Ni_{10} in the base alloy ZN07 to: Zr_9Ni_{11} with the addition of Cr, Mn, or Co; C14 with the addition of Al; and C15 with the addition of Fe. Partial replacement by Cu does not change the crystal structure, as the Zr_7Cu_{10} intermetallic compound is the only congruent solidification among the Zr_7X_{10} alloys (X = Cr, Mn, Fe, Co, Ni, or Al) according to the summary of the phase diagrams of A_7B_{10} alloys in Table 2. Therefore, the Zr_7Ni_{10} structure is preserved with partial Cu replacement (sample Cu1 and sample Cu2) while substitutions with other elements change the dominant crystal structure. This is in agreement with previous work [36,37]. Zhang et al. reported that the non-Laves Zr–Ni secondary phase evolves from Zr_7Ni_{10} to Zr_9Ni_{11} and finally to ZrNi structure as the amount of Ni-content in $Zr(Mn_{1-x}Ni_x)_2$ decreases [38,39]. In the transition between two structures, a mixture of two Zr–Ni phases can be seen, but never three phases. This observation is in agreement with our findings. According to Table 1, the available combinations of non-Laves Zr–Ni phases are Zr_7Ni_{10}, $Zr_7Ni_{10} + Zr_9Ni_{11}$, Zr_9Ni_{11}, and Zr_9Ni_{11} + ZrNi. One major difference between the Laves phase and the non-Laves Zr–Ni phase is the solubility of vanadium: both Zr_7Ni_{10} and Zr_9Ni_{11} phases have very limited solubility of vanadium [15]. According to the Ni–V–Zr ternary phase diagram giving by Gupta, only $ZrNi_3$ and $ZrNi_5$ have limited solubility of vanadium (up to 5 at.%) while other non-Laves phases have no vanadium solubility as in the case of pure zirconium [40].

The lattice constants of substituted alloys were then compared to the original values of the base alloy. With the substitution of nickel by larger elements, such as Cr, Mn, Cu, and Al, the lattice constants of all phases increase. (For the atomic radii of metals in Laves phase alloy, see Ref. [18]) Substitution of cobalt, which is the closest in size to Ni, does not change the lattice constants. However, the iron substitution is interesting as smaller amount of iron (sample Fe1) increases the lattice constant, but a larger amount of iron (sample Fe2) reduces the lattice constant. In the literature, the partial replacement of nickel by iron in AB_5 [41], C14 [42], or

Table 1
Structural properties of $Ti_{1.5}Zr_{5.5}V_{0.5}M_xNi_{9.5-x}$ alloys determined by XRD.

Alloy name	Formula	XRD phases before PCT	*a* (in Å)	*b* (in Å)	*c* (in Å)	Unit cell volume (Å^3)	Abundance (%)	XRD phases after PCT	*a* (in Å)	*b* (in Å)	*c* (in Å)	Abundance (%)
ZN07	$Ti_{1.5}Zr_{5.5}V_{0.5}Ni_{9.5}$	C15	7.026			347	8	C15	7.029			8
		Zr_7Ni_{10}	9.043	9.104	12.235	1007	92	Zr_7Ni_{10}	9.045	9.106	12.237	92
Cr1	$Ti_{1.5}Zr_{5.5}V_{0.5}Cr_{0.95}Ni_{8.55}$	C14	5.006		8.142	177	17	C14	5.007		8.143	17
		C15	7.055			351	21	C15	7.055			21
		Zr_9Ni_{11}	9.756		6.514	620	62	Zr_9Ni_{11}	9.756		6.514	62
Cr2	$Ti_{1.5}Zr_{5.5}V_{0.5}Cr_{1.9}Ni_{7.6}$	C14	5.008		8.156	177	42	C14–H	5.223		8.626	42
		Zr_9Ni_{11}	9.761		6.522	621	39	$Zr_9Ni_{11}H_x$	10.077		6.713	39
		ZrNi	3.226	9.887	4.063	130	19	$ZrNiH_x$	3.461	10.534	4.346	19
Mn1	$Ti_{1.5}Zr_{5.5}V_{0.5}Mn_{0.95}Ni_{8.55}$	C14	5.005		8.145	177	13	C14	5.007		8.147	6
								C14–H	5.221		8.624	7
		C15	7.048			350	39	C15	7.048			15
								C15–H	7.434			24
		Zr_9Ni_{11}	9.755		6.523	621	48	Zr_9Ni_{11}	9.755		6.524	16
								$Zr_9Ni_{11}H_x$	10.079		6.715	32
Mn2	$Ti_{1.5}Zr_{5.5}V_{0.5}Mn_{1.9}Ni_{7.6}$	C14	5.003		8.146	177	49	C14	5.003		8.146	38
								C14–H	5.222		8.621	11
		C15	7.054			351	17	C15	7.054			17
		Zr_9Ni_{11}	9.762		6.517	621	33	$Zr_9Ni_{11}H_x$	10.069		6.705	34
Fe1	$Ti_{1.5}Zr_{5.5}V_{0.5}Fe_{0.95}Ni_{8.55}$	C15	7.034			348	51	C15	7.034			32
								C15–H	7.432			19
		Zr_7Ni_{10}	9.085	9.149	12.249	1018	27	$Zr_7Ni_{10}H_x$	9.241	9.303	12.302	27
		Zr_9Ni_{11}	9.756		6.525	621	22	$Zr_9Ni_{11}H_x$	10.081		6.717	22
Fe2	$Ti_{1.5}Zr_{5.5}V_{0.5}Fe_{1.9}Ni_{7.6}$	C15	7.023			346	62	C15	7.023			44
								C15–H	7.429			18
		Zr_9Ni_{11}	9.754		6.523	621	38	$Zr_9Ni_{11}H_x$	10.075		6.711	38
Co1	$Ti_{1.5}Zr_{5.5}V_{0.5}Co_{0.95}Ni_{8.55}$	C15	7.021			346	33	C15	7.021			11
								C15–H	7.434			22
		Zr_7Ni_{10}	9.043	9.104	12.235	1007	31	$Zr_7Ni_{10}H_x$	9.242	9.305	12.534	31
		Zr_9Ni_{11}	9.755		6.524	621	36	$Zr_9Ni_{11}H_x$	10.019		6.725	36
Co2	$Ti_{1.5}Zr_{5.5}V_{0.5}Co_{1.9}Ni_{7.6}$	C15	7.022			346	47	C15	7.021			36
								C15–H	7.434			11
		Zr_7Ni_{10}	9.042	9.103	12.233	1007	17	$Zr_7Ni_{10}H_x$	9.242	9.305	12.534	17
		Zr_9Ni_{11}	9.756		6.524	621	36	$Zr_9Ni_{11}H_x$	10.019		6.724	36
Cu1	$Ti_{1.5}Zr_{5.5}V_{0.5}Cu_{0.95}Ni_{8.55}$	C14	5.011		8.147	348	9	C14	5.011		8.147	9
		Zr_7Ni_{10}	9.057	9.119	12.254	1012	91	Zr_7Ni_{10}	9.083	9.147	12.287	45
								$Zr_7Ni_{10}H_x$	9.253	9.317	12.547	46
Cu2	$Ti_{1.5}Zr_{5.5}V_{0.5}Cu_{1.9}Ni_{7.6}$	C14	5.013		8.151	349	11	C14	5.013		8.151	11
		Zr_7Ni_{10}	9.066	9.128	12.265	1015	89	$Zr_7Ni_{10}H_x$	9.259	9.328	12.557	89
Al1	$Ti_{1.5}Zr_{5.5}V_{0.5}Al_{0.95}Ni_{8.55}$	C14	5.018		8.156	178	34	C14–H	5.158		8.416	32
		Zr_7Ni_{10}	9.099	9.158	12.307	1026	36	$Zr_7Ni_{10}H_x$	9.242	9.305	12.534	36
		Zr_9Ni_{11}	9.805		6.574	632	32	$Zr_9Ni_{11}H_x$	10.075		6.785	32
Al2	$Ti_{1.5}Zr_{5.5}V_{0.5}Al_{1.9}Ni_{7.6}$	C14	5.058		8.216	182	67	C14–H	5.208		8.416	67
		Zr_9Ni_{11}	9.815		6.585	634	33	$Zr_9Ni_{11}H_x$	10.015		6.755	33

Table 2
Summary of phase diagram at 41% Ti or Zr, and 59% X, where X = Cr, Mn, Fe, Co, Ni, Cu, and Al. * denotes Pearson symbol. Data are from Ref. [35].

Composition	Solid type	Crystal structure during cooling	Melting temp. or eutectic temp. (°C)
$Ti_{41}Cr_{59}$	Eutectic of Ti and $TiCr_2$	*A*3 and *C*15	667
$Zr_{41}Cr_{59}$	Eutectic of Zr and ZrCr2	*A*3 and *C*15	836
$Ti_{41}Mn_{59}$	Eutectoid of TiMn and $TiMn_2$	*t**58* and *C*14	1200
$Zr_{41}Mn_{59}$	Eutectic of Zr and ZrMn2	*A*3 and *C*14	790
$Ti_{41}Fe_{59}$	Eutectic of Ti and TiFe	*A*3 and *B*2	595
$Zr_{41}Fe_{59}$	Eutectic of Zr_3Fe and $ZrFe_2$	$E1_\alpha$ and *C*15	~300
$Ti_{41}Co_{59}$	Peritectic of $TiCo_2$	*C*15	1235
$Zr_{41}Co_{59}$	Eutectic of Zr_2Co and ZrCo	*C*15 and *B*2	1312
$Ti_{41}Ni_{59}$	Eutectic of TiNi and $TiNi_3$	*B*2 and *hP*16* mixture	1118
$Zr_{41}Ni_{59}$	Peritectoid of Zr_7Ni_{10}	*oC*68*	1070
$Ti_{41}Cu_{59}$	Eutectoid of Ti_2Cu_3 and $TiCu_4$	*tP*10* and *oP*20*	870
$Zr_{41}Cu_{59}$	Congruent	*oC*68*	895
$Ti_{41}Al_{59}$	Peritectoid of $TiAl_2$	*oC*12*	1240
$Zr_{41}Al_{59}$	Peritectoid of ZrAl	B_f	1275

C15 AB_2 [43] causes the unit cells to expand. The mechanism of the lattice contraction with Fe in the current study is not presently understood. The lattice constants for the hydride phases follow the same trend as those as-prepared samples when Fe is added into the composition.

The lattice constants of Zr_9Ni_{11} phases of most alloys with transition metal substitution of Ni are very similar with the unit cell volumes being between 620 and 621 Å^3. In the case of Al substitution, the unit cell volume of Zr_9Ni_{11} goes up to 632 (sample Al1) and 634 Å^3 (sample Al2). Zhang et al. reported that the lattice constants of Zr_9Ni_{11} change in $Zr(Mn_xV_{0.45-x}Ni_{0.55})_2$ alloys but the change is not associated with the change in the average atomic radius of B atoms [44]. The determining factor with respect to the lattice constants of Zr_9Ni_{11} remains a subject for further investigation.

The relative phase abundances are plotted against the amount of substitution in Fig. 2. The abundance of C14 phase increases rapidly with substitutions of Al, Mn, and Cr, and is believed to be associated with the lower number of valance electrons of the substituting elements (Fig. 2a). The C15 phase dominates with substitutions of Fe and Co, which is in agreement with the prediction from research on $ZrMn_2$ based alloys [31]. The initial increase and subsequent decrease in C15 phase abundance with the substitution of Mn and Cr (Fig. 2b) is discussed in the EDS results section. As stated before, except for Cu substitution, the Zr_7Ni_{10} phase decreases dramati-

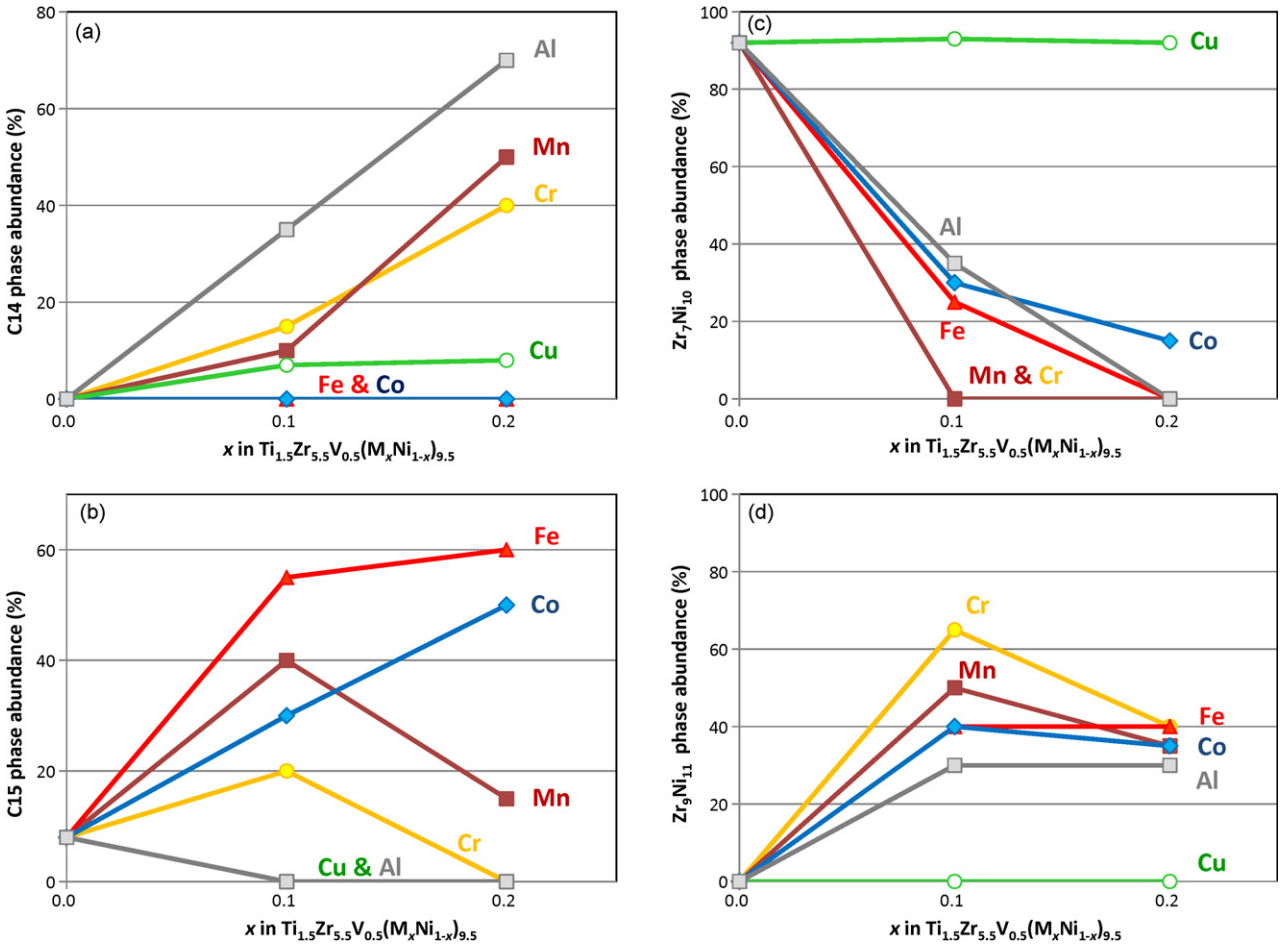

Fig. 2. The evolution of C14 (a), C15 (b), Zr_7Ni_{10} (c), and Zr_9Ni_{11} (d) phase abundance as functions of the *x* value in alloys $Ti_{1.5}r_{5.5}V_{0.5}(M_xNi_{1-x})_{9.5}$.

cally with the increasing substitution (Fig. 2c). As for the abundance of Zr_9Ni_{11} phase, all non-Cu substitutions show initial increases and then converge to a narrow range between 30% and 40% as the amount of substitution increases (Fig. 2d). The reason for this convergence requires further investigation.

Partially hydrided samples were prepared by fully hydriding the alloys to 2 MPa of hydrogen and then pumping down to an equilibrium hydrogen pressure at 1 kPa. Some hydrogen remains in the phases which have an equilibrium pressure lower than 1 kPa. Samples were taken out of the PCT apparatus and put in the XRD instrument immediately. The resulting XRD spectra are shown in Fig. 3 and summarized in Table 1. In Fig. 3, the hydride β-phases are in lighter gray color while the original α-phases are in black. In the case of Cr substitution, sample Cr1 shows a complete dehydride without any significant changes in lattice constants while sample Cr2 shows measurable expansion of all three constituent phases. The percentages of volume expansion in decreasing order are ZrNi (22%), C14 (15%), and Zr_9Ni_{11} (10%). The expansion of the ZrNi phase is the largest. In the case of sample Mn1, all three phases become partially hydrided, and the percentages of volume expansion in decreasing order are C15 (17%), C14 (15%), and Zr_9Ni_{11} (10%). As the Mn amount increases (sample Mn2), the hydrogen storage in C15 phase becomes totally reversible and in the Zr_9Ni_{11} phase becomes totally irreversible, and more hydrogen in the C14 phase is released. In the case of Fe and Co substitutions, C15 becomes partially dehydrided while Zr_7Ni_{10} and Zr_9Ni_{11} remained completely dehydrided. The percentages of volume expansion in decreasing order are C15 (18–19%), Zr_9Ni_{11} (9–10%), and Zr_7Ni_{10} (4–7%). In the case of Cu substitution, the C14 phase is totally reversible while the Zr_7Ni_{10} changes from being partially reversible to being totally irreversible as the Cu amount increases. Although Cu preserves the Zr_7Ni_{10} crystal structure, it is detrimental to hydrogen storage reversibility. Finally, in the case of Al substitution, all phases remain hydrided after PCT analysis with the volume expansion in decreasing order of C14 (9%), Zr_9Ni_{11} (7–9%), and Zr_7Ni_{10} (5%). In general, the hydride lattice expansion is in the order of ZrNi (22%), C15 (17–19%), C14 (9–15%), Zr_9Ni_{11} (7–10%), and Zr_7Ni_{10} (4–7%). This is equivalent to the order of hydrogen intake of alloys under the assumption that the hydrogen occupancy is the only reason for the lattice expansion.

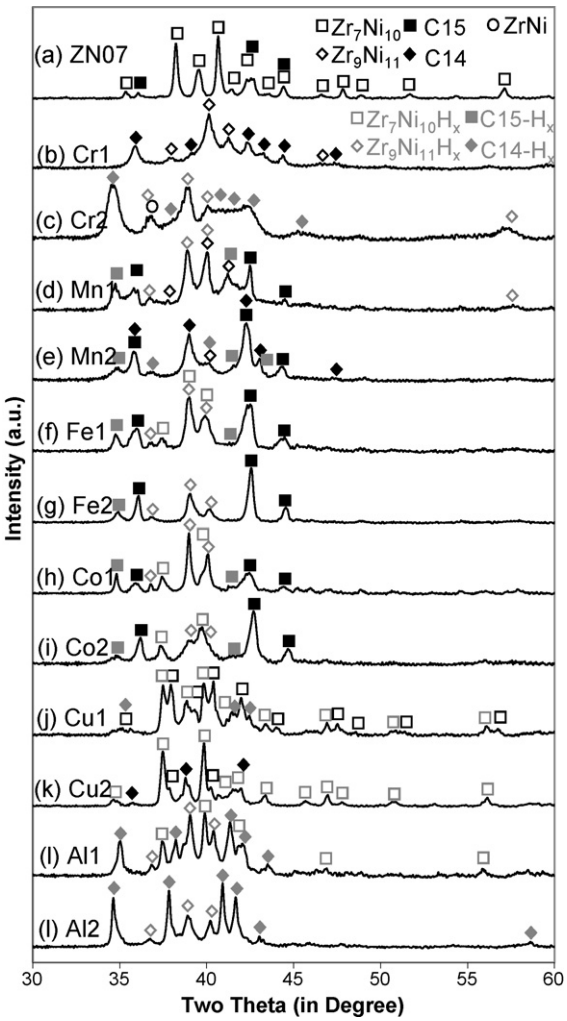

Fig. 3. XRD spectra using Cu Kα as the radiation source for after-PCT alloys ZN07 (a), Cr1 (b), Cr2 (c), Mn1 (d), Mn2 (e), Fe1 (f), Fe2 (g), Co1 (h), Co2 (i), Cu1 (j), Cu2 (k), Al1 (l), and Al2 (m). The black and gray symbols are for α and β phases of the hydrides, respectively.

3.2. Microstructures observed by SEM/EDS

In order to understand the various phase formations during solidification with different substitution elements, the phases of A_7B_{10} and AB_2 compositions from A–B binary phase diagrams are summarized in Tables 2 and 3. Most of the A_7B_{10} alloys do not solidify congruently except for Zr_7Cu_{10}. None of the other substitution elements has a solidification product with a Zr_7X_{10} crystal structure, which is why the phase abundance of Zr_7Ni_{10} drops substantially with any non-Cu substitution (Fig. 2c). As for the AB_2 composition listed in Table 3, most of the intermetallic alloys are AB_2 from congruent solidification or peritectic reaction with the exception of $TiCu_2$ ($r_A/r_B = 1.14$) and $TiAl_2$ ($r_A/r_B = 1.02$) where the radius ratios between the A and B atoms are below the threshold of Laves phase [45]. $ZrCu_2$ is another exception due to the existence

Table 3
Summary of phase diagram at 33% Ti or Zr, and 67% X, where X = Cr, Mn, Fe, Co, Ni, Cu, and Al. * denotes Pearson symbol. Data are from Ref. [35].

Composition	Solid type	Crystal structure during cooling	Solubility of X	Melting temp. or eutectic temp. (°C)
$Ti_{33}Cr_{67}$	Congruent	BCC–C36–C14–C15	Med. (63–65%)	1370
$Zr_{33}Cr_{67}$	Congruent	C14–C36–C15	Large (64–69%)	1673
$Ti_{33}Mn_{67}$	Congruent	C14	Very Large (60–70%)	1325
$Zr_{33}Mn_{67}$	Congruent	C14	Very Large (60–79%)	1450
$Ti_{33}Fe_{67}$	Congruent	C14	Large (65–72%)	1427
$Zr_{33}Fe_{67}$	Congruent	C15	Large (66–73%)	1673
$Ti_{33}Co_{67}$	Peritectic	C15	Small (66.5–67%)	1235
$Zr_{33}Co_{67}$	Congruent	C15	Large (65–73%)	1560
$Ti_{33}Ni_{67}$	Eutectic of TiNi and $TiNi_3$	B2 and $hP16^*$ mixture		1118
$Zr_{33}Ni_{67}$	Eutectic of Zr_7Ni_{10} and Zr_8Ni_{21}	$oC68^*$ and triclinic		1070
$Ti_{33}Cu_{67}$	Eutectic of Ti_2Cu_3 and $TiCu_4$	$tP10^*$ and $oP20^*$		870
$Zr_{33}Cu_{67}$	Eutectic of Zr_7Cu_{10} and Zr_3Cu_8	$oC68^*$ and $oP44^*$		885
$Ti_{33}Al_{67}$	Peritectoid	$oC12^*$	Narrow	1240
$Zr_{33}Al_{67}$	Congruent	C14	Narrow	1645

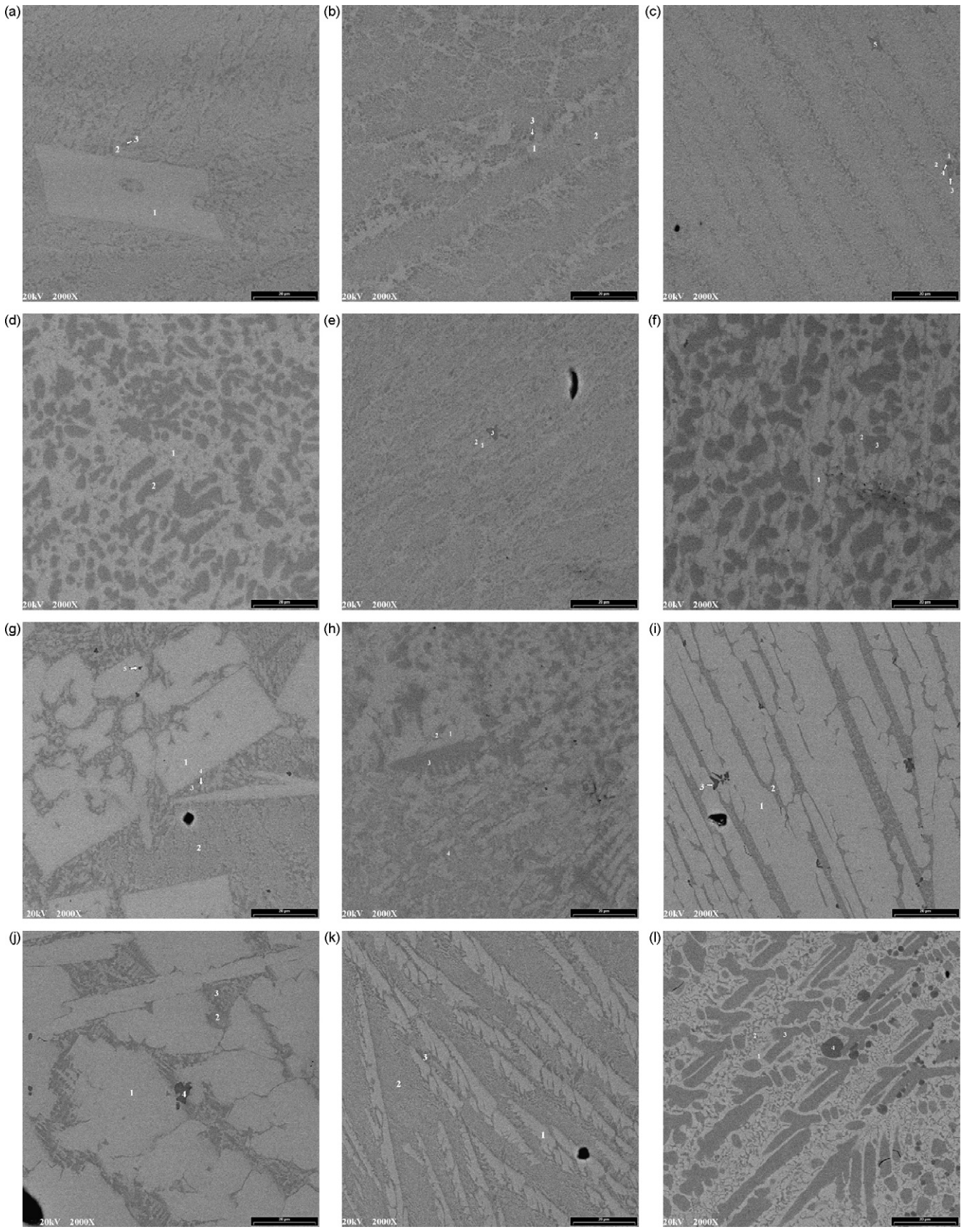

Fig. 4. SEM backscattering electron image micrographs for alloys Cr1 (a), Cr2 (b), Mn1 (c), Mn2 (d), Fe1 (e), Fe2 (f), Co1 (g), Co2 (h), Cu1 (i), Cu2 (j), Al1 (k), and Al2 (l). The bar on the right lower corner indicates a length of 20 μm. Compositions identified in the micrograph by EDS analysis are listed in Table 4.

of a more stable Zr_7Cu_{10} phase. According to the phase diagrams of $TiCr_2$ and $ZrCr_2$, C14 phase has a higher melting temperature than the C15 and should solidify first during cooling. This cooling sequence has been confirmed by SEM/TEM studies published elsewhere [46,47].

Fig. 4a-l shows the SEM–BEI micrographs for all 12 substituted alloys at the same magnification. The chemical compositions of the areas labeled with reference numerals were analyzed by EDS and the results are summarized in Table 4. The B-to-A ratio, average electron density (e/a value), and the phase identification are also included. The B-to-A ratio was calculated based on the assumption that only Zr and Ti occupy the A-site while all other elements in this study occupy the B-site due to their relatively small atomic sizes. A previous study of partial replacement of Ni by Al in C14 alloy did not show a clear trend of changes in lattice size and therefore the precise site for Al could not be determined [20]. However, from the Nb–Ni–Al ternary phase diagram, C14 phase seems to have a wide composition range with Al in the B-site [48]. The occupation of V in the B-site of a C14-dominated alloy was confirmed before by XRD analysis [49]. All other smaller elements should substitute for Ni in the B-site.

The percentage of C15 in the overall AB_2 alloy is plotted against the e/a value of the identified AB_2 Laves phase in Fig. 5. Except for data from sample Cu1 and sample Cu2 where the AB_2 contents are relatively small (9–11%) and where C15 is difficult to be resolved from the XRD spectrum, the $C15/AB_2$ ratio shows a good dependency on e/a value, which has been demonstrated many times before in the literature [50–55]. The threshold of e/a value for C14/C15 transition is about 6.9–7.0, which is close to the value of 7.1 reported by Chao et al. in a series of similar alloys of high degree in disorder [52].

3.2.1. *Base $Ti_{1.5}Zr_{5.5}V_{0.5}Ni_{0.95}$ alloy*

The SEM–BEI micrograph of ZN07 is shown in Fig. 3b in Ref. [15]. It shows a typical acicular structure from a eutectic solidification [56]. Recently, this type of dendrite growth has been simulated suc-

Table 4
Summary of EDS chemical composition in micrographs Fig. 3a-l. Numbers are in atomic percentage. Row begins with a * symbol represents the calculated composition based on the abundance from XRD analysis and composition of other phases. e/a value is the average electron density based on the atomic percentage and the number of outer shell electrons of constituent element.

	Zr	Ti	Ni	V	M	(NiVM)/(ZrTi)	e/a value	Phase
Cr1-1	39.0	6.1	54.3	0.3	0.3	1.22		Zr_9Ni_{11}
Cr1-2	36.1	10.2	52.3	0.7	0.6	1.16		Zr_9Ni_{11}/AB_2 mixture
Cr1-3	30.4	8.1	48.1	6.7	6.7	1.60	7.09	AB2
Cr2-1	38.2	7.4	53.6	0.4	0.4	1.19		Zr_9Ni_{11}
Cr2-2	34.2	9.4	47.8	3.4	5.2	1.29		Zr_9Ni_{11}/AB_2 mixture
Cr2-3	35.9	9.8	49.0	2.1	3.2	1.19		ZrNi
*	24.6	9.7	33.7	5.9	26	1.91	6.60	AB_2 (calculated from abundance)
Mn1-1	33.7	9.0	54.7	0.3	2.2	1.34		Zr_9Ni_{11}
Mn1-2	34.3	8.8	48.7	2.8	5.4	1.32		Zr_9Ni_{11}/AB_2 mixture
Mn1-3	35.0	6.8	29.2	11.3	17.7	1.39		AB_2/Zr_9Ni_{11} mixture
Mn1-4	63.3	6.0	26.2	1.0	3.5	0.44		ZrO_2/Zr_9Ni_{11} mixture
Mn1-5	89.0	3.3	7.0	0.2	0.5	0.08		ZrO_2
*	32.3	8.8	50.3	2.94	5.6	1.53	7.21	AB_2 (calculated from abundance)
Mn2-1	37.3	10.4	47.4	0.4	4.6	1.10		Zr_9Ni_{11}
Mn2-2	29.4	7.5	35.4	7.1	20.7	1.71	6.82	AB_2
Fe1-1	36.2	8.6	49.1	1.9	4.2	1.23		$Zr_9Ni_{11}/Zr_7Ni_{10}/AB_2$
Fe1-2	34.3	9.0	50.7	1.7	4.3	1.31		$Zr_9Ni_{11}/Zr_7Ni_{10}/AB_2$
Fe1-3	93.9	2.2	3.5	0.1	0.3	0.04		ZrO_2
*	42.5	8.2	47.2	0.3	1.9	0.97		Zr_9Ni_{11}/Zr_7Ni_{10} (calculated)
*	23.9	9.2	52.9	5.0	8.6	2.00	7.56	AB_2 (calculated)
Fe2-1	39.7	6.9	51.7	0.0	1.7	1.15		Zr_9Ni_{11}
Fe2-2	34.9	14.1	44.5	0.8	5.7	1.04		ZrNi
Fe2-3	29.4	6.4	30.9	6.5	26.9	1.80	7.00	AB_2
Co1-1	38.4	7.1	50.0	0.8	3.7	1.20		Zr_9Ni_{11}
Co1-2	32.0	9.4	48.6	4.2	5.9	1.42		Zr_7Ni_{10}/AB_2 mixture
Co1-3	29.8	9.1	46.2	7.1	7.8	1.57		AB_2/Zr_7Ni_{10} mixture
Co1-4	31.5	13.4	47.5	2.1	5.5	1.23		Zr_9Ni_{11}/AB_2 mixture
Co1-5	51.1	6.6	38.4	0.7	3.2	0.73		ZrO_2
*	34.9	9.8	51.8	0.4	3.4	1.24		Zr_7Ni_{10} (calculated)
*	28.6	8.9	44.9	8.7	8.8	1.66	7.22	AB_2 (calculated)
Co2-1	35.8	7.7	49.4	0.7	6.4	1.30		Zr_9Ni_{11}
Co2-2	32.1	13.4	44.1	0.9	9.5	1.20		Zr_9Ni_{11}/Zr_7Ni_{10} mixture
Co2-3	30.3	6.6	38.8	7.6	16.7	1.71	7.24	AB_2
Co2-4	33.9	9.3	41.2	3.0	12.6	1.31		Zr_9Ni_{11}/AB_2 mixture
Cu1-1	36.3	6.7	50.6	0.8	5.6	1.33		Zr_7Ni_{10}/AB_2 mixture
Cu1-2	28.2	15.2	44.7	8.1	3.8	1.30	7.03	AB_2
Cu1-3	80.2	3.0	14.7	0.8	1.4	0.20		ZrO_2
Cu2-1	36.2	6.6	45.4	0.4	11.4	1.34		Zr_7Ni_{10}
Cu2-2	27.7	18.1	39.5	8.5	6.3	1.19	6.90	AB_2
Cu2-3	25.7	21.2	40.4	5.4	7.4	1.13	7.00	AB_2
Cu2-4	95.1	0.6	3.2	0.3	0.8	0.04		ZrO_2
Al1-1	31.7	7.9	52.0	0.6	7.8	1.53		Zr_7Ni_{10}
Al1-2	33.5	9.5	50.8	2.7	3.3	1.32		Zr_9Ni_{11}/AB_2 mixture
Al1-3	32.8	9.3	49.7	3.7	4.4	1.38		Zr_9Ni_{11}/AB_2 mixture
*	36.1	11.6	51.4	0.3	0.3	1.18		Zr_9Ni_{11} (calculated)
*	29.5	8.3	45.7	7.5	9.0	1.64	6.72	AB_2 (calculated)
Al2-1	34.0	10.0	49.5	0.2	6.2	1.27		Zr_9Ni_{11}
Al2-2	30.4	8.6	49.1	0.3	11.7	1.57		Zr_7Ni_{10}
Al2-3	29.0	7.8	39.4	7.2	16.7	1.72	6.27	AB_2
Al2-4	19.2	6.0	49.9	0.1	24.9	2.97		$ZrNi_3$

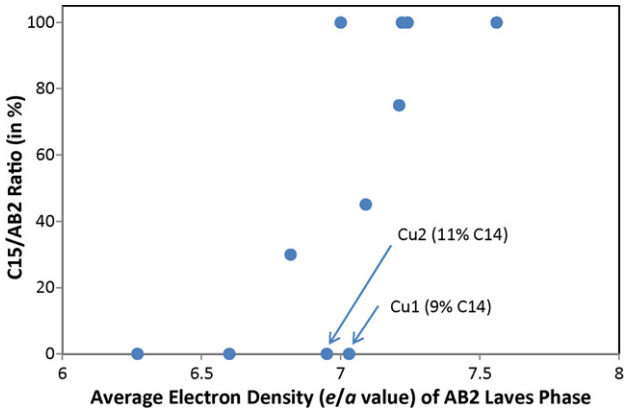

Fig. 5. The percentage of C15 phase abundance in AB_2 vs. the average electron density either measured by EDS or calculated from the XRD phase abundance.

cessfully by a phase field model [57]. The matrix in this alloy has a Zr_7Ni_{10} structure, and the dendrite is C15 phase solidified first during cooling from the liquid. The alignment of the dendrite orientation is associated with the solidification path (from the outside to the inside of the ingot).

3.2.2. Cr substitution

For sample Cr1, SEM shows a large area of Zr_9Ni_{11} phase (lighter area 1) (Fig. 4a). The rest of the area is a mixture of Zr_9Ni_{11} and AB_2 phases. Most of the substituting Cr and V are found in the AB_2 phase. The Zr_9Ni_{11} to AB_2 ratio is about 2–1, which agrees with the estimation from XRD analysis. From the microstructure, the AB_2 phase is believed to solidify first and remove all vanadium from the liquid. Zr_9Ni_{11} is the last to solidify and forms the matrix of the alloy. The e/a value calculated from the AB_2 phase is 7.09, which is slightly higher than the threshold and corresponds well with the C15-dominance found in XRD analysis.

As the Cr-content increases, the Zr_9Ni_{11} phase remains as the matrix with fine grains of AB_2 and larger grains of ZrNi included within (Fig. 4b). Very small amounts of Cr and V are found in the Zr_9Ni_{11} phase. The lattice constants of the Zr_9Ni_{11} matrix increase slightly because Cr is larger than Ni. The calculated AB_2 composition (based on phase abundance discovered by XRD analysis and Zr_9Ni_{11} composition from EDS) shows a relatively high B/A ratio of 1.90, which is very close to the ideal stoichiometry of 2.0. The average e/a value of this calculated AB_2 composition is 6.60, which is in agreement with the pure C14 phase found in XRD analysis.

3.2.3. Mn substitution

For sample Mn1, the main matrix is Zr_9Ni_{11} phase with a very small V-content and a low Mn content (Fig. 4c). Very fine grains of AB_2 are spread along what is believed to be the cooling direction. ZrO_2 is also seen in the micrograph. The composition of the AB_2 phase calculated based on the phase abundance shows a B-to-A ratio of 1.53, which indicates the existence of either anti-site disorder or under-stoichiometry. This is consistent with the wide range of C14 composition in both $TiMn_2$ and $ZrMn_2$ as indicated in Table 3. The r_A/r_B ratio of $ZrMn_2$ is 1.24, which is very close to the ideal ratio $(3/2)^{1/2} = 1.225$, and therefore the solubility of C14 phase is very high [45].

As the Mn content increases (sample Mn2), the grains of AB_2 (darker region) become much larger (Fig. 4d). The e/a ratio of the AB_2 phase is 6.82, which is just below the threshold of a C14/C15 transition and therefore agrees with the C14-dominance as discovered in XRD analysis. The matrix remains a Zr_9Ni_{11} structure and contains almost no vanadium and some Mn (still below the average). The majority of Mn is found in the AB_2 phase. Although the compositions of the Zr_9Ni_{11} phase in samples Mn1 and Mn2 are different (Zr in sample Mn2 is higher than that in sample Mn1 at the expense of Ni), the cell volume is almost the same. The reason for the volume remaining unchanged is unknown.

3.2.4. Fe substitution

The microstructure of sample Fe1 is similar to that of sample Mn1 with the Zr_7Ni_{10}/Zr_9Ni_{11} phases as the matrix and AB_2 phase as the dendrite outgrowth (Fig. 4e). The SEM resolution is not adequate to distinguish between the Zr_7Ni_{10} and Zr_9Ni_{11} phases. The estimation of AB_2 composition is more complicated than for samples Cr2 and Mn1. We first note there is at most 0.3% V in either Zr_7Ni_{10} or Zr_9Ni_{11}. Therefore, we know the content of V in AB_2 phase is about 5% judging from the 51% C15 phase abundance and 2.9% V in the design composition. In the reference numeral 1 spot of sample Fe1, the percentage of AB_2 is 34% based on the average V-content at 1.9%. For the average composition, the percentage of AB_2 is 51% with the percentage of vanadium being 5.5%. The composition of AB_2 and non-Laves phases can be calculated by solving the two-variable linear equations. The results are listed in Table 4. The AB_2 composition calculated in this way has a perfect stoichiometry (B/A = 2.0) and the e/a value is 7.56, which correlates well with the C15-only AB_2 structure. The iron content in the C15 phase is much higher than the non-Laves phase and is the main driving force to move the main phase away from the non-Laves phase.

As the Fe content increases, the grain size becomes much larger as it does for Mn (Fig. 4f) and one of the minor phase changes from Zr_7Ni_{10} to ZrNi, which agrees with the reduction in Ni-content. The V and Fe contents in the ZrNi phase are higher than those in Zr_9Ni_{11} but are still lower than the average composition. Most of the iron was found in the AB_2 phase, causing the e/a value to decrease to 7.0 since Fe has fewer outer shell electrons than the substituting Ni. The AB_2 phase remains C15-dominated with a small increase in the abundance.

3.2.5. Co substitution

The phase segregation of sample Co1 is similar to that of sample Cr1 with the main matrix being a Zr_9Ni_{11} phase (Fig. 3g). Zr_7Ni_{10} was found as the secondary phase finely mixed with the AB_2 phase (which was not observed in the case of sample Cr1). Due to the distribution of fine grains of the secondary phases, a single area for EDS analysis is not available for the Zr_7Ni_{10} and AB_2 phases. A calculation similar to the one performed on sample Fe1 was performed, and the compositions of these two phases were calculated and are listed in Table 4. Zr_7Ni_{10} has slightly lower contents of V and Co than Zr_9Ni_{11}. In both cases, while the Co content is close to the average composition, the V content is much lower than the average composition. The e/a value of the calculated composition of AB_2 is 7.22, which agrees with the pure C15 structure in the AB_2 phase.

As the Co level increases, the large area of the matrix phase disappears (as in the case of sample Cr2). The abundance of Zr_9Ni_{11} remains about the same at 36%. The abundance of Zr_7Ni_{10} is cut in half due to the reduction in Ni-content. The AB_2 phase, which contains most of the V and Co in the alloy, has an e/a value of 7.24, which is in agreement with a C15-dominated structure.‘

3.2.6. Cu substitution

Cu is a unique substitution element in this study due to the unchanged crystal structure from Zr_7Ni_{10} to Zr_7Cu_{10} [58]. From the XRD structure study, the content of Zr_7Ni_{10} remained dominant and unchanged with Cu substitution (Fig. 2). While the micrograph of sample Cu1 (Fig. 4i) shows a typical dendrite structure, sample Cu2 exhibits a morphology similar to a ternary three-phase solidification [59]. Both samples show a matrix of Zr_7Ni_{10} phase with the highest content of Cu. The e/a values calculated from the com-

position of AB_2 phase are very close to the critical point between the C14 and C15 structure. However, due to the small volume percentage of AB_2 phases in these two samples, we cannot resolve the C15 phase in the XRD analysis. We can only estimate it is a C14-dominated structure. Another point worth mentioning is the low B/A ratio in the AB_2 phase in Cu-substituted alloys (1.3 and 1.19). In this series of alloys, most of the B/A ratios of AB_2 phase are in the range between 1.6 and 1.8. Some anti-site and vacancy defects are expected. However, the deviation from the ideal B/A ratio is very large for samples Cu1 and Cu2, which will be further investigated in the future.

3.2.7. Al substitution

The microstructure of sample Al1 is composed of a Zr_7Ni_{10} matrix and dendrites made from a fine mixture of Zr_9Ni_{11} and AB_2 (Fig. 3k). The compositions of the Zr_9Ni_{11} and AB_2 phases are calculated from the EDS data of two Zr_9Ni_{11}/AB_2 mixed area under the assumption that there is no Zr_7Ni_{10} in the mixed areas. The percentages of Zr_9Ni_{11} in the areas of sample Al1 having reference numerals 2 and 3 are 66% and 53%, respectively. The calculated B/A ratio for Zr_9Ni_{11} is 1.18, which is very close to the stoichiometric ratio of 11/9 = 1.22. The e/a value of AB_2 is 6.72, which agrees with the C14-dominated microstructure.

As the amount of Al-substitution increases, the AB_2 grain grows larger in size and a new phase with a composition close to $ZrNi_3$ is found (Fig. 3l). This new phase has the highest content of Al and almost no V. The AB_2 phase has an e/a value of 6.27 and correlates well with the dominance of the C14 structure.

4. Summary

The results of this study on the microstructure of series of alloys with the substitution in Ni in the base alloy $Ti_{1.5}Zr_{5.5}V_{0.5}Ni_{9.5}$ are summarized below.

Base alloy: Zr_7Ni_{10} matrix with C15 dendrites.
Cr substitution: Zr_9Ni_{11} matrix with C14/C15 (sample Cr1) and C14/ZrNi fine grains (sample Cr2).
Mn substitution: Zr_9Ni_{11} matrix with C14/C15 fine grains (sample Mn1) and large grains (sample Mn2).
Fe substitution: Fine grains mixture (sample Fe1) and larger grains (sample Fe2) of C15, Zr_9Ni_{11} and Zr_7Ni_{10} phases.
Co substitution: Zr_9Ni_{11} matrix with Zr_7Ni_{10}/C15 fine grains.
Cu substitution: Zr_7Ni_{10} matrix with C14 dendrites.
Al substitution: Zr_7Ni_{10} matrix with Zr_9Ni_{11}/C14 dendrites (sample Al1) and Zr_9Ni_{11} matrix with large grains of C14 and $ZrNi_3$, and small grains of Zr_7Ni_{10} (sample Al2).

References

[1] S. Wakao, Y. Yonemura, H. Nakano, H. Shimada, J. Less-Common Met. 104 (1984) 365.
[2] S. Wakao, H. Sawa, H. Nakano, S. Chubachi, M. Abe, J. Less-Common Met. 131 (1987) 311.
[3] H. Sawa, K. Ohzeki, M. Ohta, H. Nakano, S. Wakao, Z. Phys. Chem. Neue Folge Bd. 164S (1989) 1521.
[4] H. Sawa, M. Ohta, H. Nakano, S. Wakao, Z. Phys. Chem. Neue Folge Bd. 164S (1989) 1527.
[5] J.M. Joubert, R. Cerný, K. Yvon, M. Latroche, A. Percheron-Guégan, Acta Crystallogr. C53 (1997) 1536.
[6] I. Noriyasu, Japan Patent Hei 6-57358 (1994).
[7] J.M. Joubert, M. Latroche, A. Percheron-Guégan, J. Alloys Compd. 231 (1995) 494.
[8] J.Y. Yu, Y.Q. Lei, C.P. Chen, J. Wu, Q.D. Wang, J. Alloys Compd. 231 (1995) 578.
[9] M.E. Badding, M.T. McCormack, D.W. Murphy, B. Vyas, US Patent 5,560,752 (1996).
[10] J.M. Joubert, M. Latroche, A. Percheron-Guégan, J. Bouet, J. Alloys Compd. 240 (1996) 219.
[11] F.C. Ruiz, E.B. Castro, S.G. Real, H.A. Peretti, A. Visintin, W.E. Triaca, Int. J. Hydrogen Energy 33 (2008) 3576.
[12] F.H.M. Spit, J.W. Drijver, W.C. Turkenburg, S. Radelaar, J. Phys. 41 (1980) C8–C890.
[13] F.H.M. Spit, J.W. Drijver, S. Radelaar, Scr. Metall. 14 (1980) 1071.
[14] K. Young, T. Ouchi, Y. Liu, B. Reichman, W. Mays, M.A. Fetcenko, J. Alloys Compd. 480 (2009) 521.
[15] K. Young, T. Ouchi, M.A. Fetcenko, W. Mays, B. Reichman, Int. J. Hydrogen Energy 34 (2009) 8695.
[16] K. Young, J. Nei, B. Huang, T. Ouchi, M.A. Fetcenko, J. Alloys Compd 501 (2010) 245.
[17] K. Young, T. Ouchi, M.A. Fetcenko, J. Alloys Compd. 476 (2009) 774.
[18] K. Young, T. Ouchi, J. Koch, M.A. Fetcenko, J. Alloys Compd. 477 (2009) 749.
[19] K. Young, T. Ouchi, B. Reichman, W. Mays, M.A. Fetcenko, R.K. Regmi, G. Lawes, A. Wu, J. Alloys Compd. 489 (2010) 202.
[20] K. Young, T. Ouchi, M.A. Fetcenko, R.K. Regmi, G. Lawes, J. Alloys Compd. 490 (2010) 282.
[21] K. Young, M.A. Fetcenko, J. Koch, K. Morii, T. Shimizu, J. Alloys Compd. 486 (2009) 559.
[22] K. Oguro, M. Tanaka, US. Patent 5,100,615 (1992).
[23] A. Drašner, Ž. Blažina, J. Less-Common Met. 175 (1991) 103.
[24] B. Liu, D. Kim, K. Lee, J. Lee, J. Alloys Compd. 240 (1996) 214.
[25] B.K. Singh, S. Cho, H. Yoon, C. Kim, K. Bartwal, Mater. Chem. Phys. 112 (2008) 686.
[26] J. Park, H. Jang, S. Han, P. Lee, J. Lee, J. Alloys Compd. 325 (2001) 293.
[27] M. Bououdina, J.L. Soubeyroux, D. Fruchart, Int. J. Hydrogen Energy 22 (1997) 329.
[28] Y. Yamamura, H. Seri, Y. Tsuji, N. Owada, T. Iwaki, US Patent 5,532,076 (1996).
[29] Y. Izumi, Y. Moriwaki, K. Yamashita, T. Tokuhiro, US Patent 5,962,156 (1999).
[30] S. Han, M. Zhao, L. Wu, Y. Zheng, Chem. J. Chin. Univ. 24 (2003) 2256.
[31] W. Zhang, C. Ma, H. Huang, X. Yang, Y. Lei, Q. Wang, Chin. J. Nonferr. Met. 12 (2002) 897.
[32] Y. Osumi, H. Suzuki, A. Kato, K. Oguro, S. Kawai, M. Kaneko, J. Less-Common Met. 89 (1983) 287.
[33] M.A. Fetcenko, S.R. Ovshinsky, K. Young, R. Benjamin, T. Ouchi, J. Koch, W. Mays, US Patent 6,830,725 (2004).
[34] T. Kabutomori, Y. Wakisaka, K. Tsuchiya, H. Kawamura, J. Nucl. Mater. 258–263 (1998) 481.
[35] T.B. Massalski, Binary Alloy Phase Diagram, ASM International, Ohio, USA, 1990.
[36] J.L. Glimois, P. Forey, J. Feron, C. Becle, J. Less-Common Met. 78 (1981) 45.
[37] L. Bsenko, J. Less-Common Met. 40 (1975) 365.
[38] W. Zhang, C. Ma, X. Yang, Y. Lei, Q. Wang, G. Li, Rare Met. Mater. Eng. 28 (1999) 202.
[39] X. Hu, J. Gu, L. Chen, G. Lu, W. Zhang, Y. Lei, Q. Wang, Chin. J. Mater. Res. 13 (1999) 129.
[40] K.P. Gupta, J. Phase Equil. 21 (2000) 88.
[41] R.K. Singh, M.V. Lototsky, O.N. Srivastava, Int. J. Hydrogen Energy 32 (2007) 2971.
[42] M.Y. Song, D. Ahn, I. Kwon, R. Lee, H. Rim, J. Alloys Compd. 298 (2000) 254.
[43] A. Jain, R.K. Jain, S. Agarwal, V. Ganesan, N.P. Lalla, D.M. Phase, I.P. Jain, Int. J. Hydrogen Energy 32 (2007) 3965.
[44] W. Zhang, C. Ma, H. Hui, X. Yang, J. Tu, Y. Lei, Rare Met. Mater. Eng. 30 (2001) 194.
[45] D.J. Thoma, J.H. Perepezko, J. Alloys Compd. 224 (1995) 330.
[46] Y. Liu, K. Young, private communication.
[47] W.J. Boettinger, D. E. Newbury, K. Wang, L.A. Bendersky, C. Chiu, U.R. Kattner, K. Young, B. Chao, Metallur. Mater. Trans. (in press).
[48] L. Machon, G. Sauthoff, Intermetallics 4 (1996) 469.
[49] K. Young, M.A. Fetcenko, F. Li, T. Ouchi, J. Koch, J. Alloys Compd. 468 (2009) 482.
[50] J.H. Zhu, P.K. Liaw, C.T. Liu, Mater. Sci. Eng. A239–240 (1997) 260.
[51] J.H. Zhu, C.T. Liu, P.K. Liaw, Intermetallics 7 (1999) 1011.
[52] B.S. Chao, R.C. Young, S.R. Ovshinsky, D.A. Pawlik, B. Huang, J.S. Im, B.C. Chakoumakos, in: D. Doughty, L. Nazar, M. Arakawa, H.-P. Brack, K. Naoi (Eds.), Mater. Res. Soc. Symp. Proc., vol. 575, Warrendale, PA, 1999, p. 193.
[53] Z. Shi, S. Chumbley, F.C. Laabs, J. Alloys Compd. 312 (2000) 41.
[54] F. Stein, M. Palm, G. Sauthoff, Intermetallics 12 (2004) 713.
[55] S. Amerioun, T. Yokosawa, S. Lidin, U. Häussermann, Inorg. Chem. 43 (2004) 4751.
[56] F.N. Rhines, Phase Diagrams in Metallurgy, McGraw-Hill Book Company, New York, 1956, p. 39.
[57] Y. Zhao, H. Hou, J. Phys.: Conf. Ser. 29 (2006) 210.
[58] C. Liu, W. Chiang, K. Hsieh, Y. Chang, Intermetallics 14 (2006) 1011.
[59] F.N. Rhines, Phase Diagrams in Metallurgy, McGraw-Hill Book Company, New York, 1956, p. 135.